Supplementary Material for

Supershear-subshear-supershear rupture sequence during the 2025 Mandalay Earthquake in Myanmar

Shiro Hirano*[1], Ryosuke Doke[1], and Takuto Maeda[1]

[1]Hirosaki University, 3, Bunkyo, Hirosaki City, Aomori, 036-8561, Japan

July 30, 2025

Abstract

This material details the methodologies used in the main text.

S1 Methods

S1.1 Image analysis to extract slip history from the video

In the initial analysis of the video (Hirano, 2025), the author executed the following steps as shown in Fig.S1:

- Step 1: A 100×20 px region, starting 152 px from the top and 930 px from the left, in video frames was cropped from each video frame.
- Step 2: The cropped images were compressed vertically to 100×1 px, to obtain a vertical average.
- Step 3: Edges in the 1-px-height images were enhanced.
- Step 4: The distance between the leftmost and rightmost white pixels was measured.

S1.2 Calculations to obtain the deceleration point and subshear rupture velocity

The initial supershear rupture velocity V_{sup} falls between V_P (= 6.0 km/s) and V_S (= 3.5 km/s). At the CCTV site, from the video frames, the P-wave duration τ_P is, though uncertain, at least 3 seconds, while S-wave duration τ_S is approximately 2 seconds. The S-wave front arrival time therein is $t_C^S := V_P^{-1} r_C + \tau_P$, and the equation of the front (gray dotted line in Fig.S2a) is given by

$$r = V_S \left(t - t_C^S\right) + r_C.$$

The intersection of this line and the initial rupture propagation represented by $r = V_{\mathrm{sup}} t$ gives the deceleration point which is the origin of the observed S-wave. The solution r_d is calculated as:

$$r_d = \frac{r_C - V_S t_C^S}{1 - V_S / V_{\mathrm{sup}}}.$$

The subshear rupture velocity V_{sub} from the deceleration point to CCTV is

$$V_{\mathrm{sub}} = \frac{r_C - r_d}{t_C^S + \tau_S - r_d / V_{\mathrm{sup}}},$$

*hirano@hirosaki-u.ac.jp

where $t_C^S + \tau_S$ and $r_d/V_{\rm sup}$ in the denominator represent the rupture times at the CCTV and the deceleration point, respectively. From the above, unknown parameters are τ_P and $V_{\rm sup}$. Given that rupture reached $r = r_N$ at $t = t_N$, the following condition must be satisfied:

$$t_C^S + \tau_S \leq t_N - \frac{r_N - r_C}{V_P}. \tag{S.1}$$

where the right-hand side denotes the boundary between the white and top-right gray regions in Fig.S2a. Otherwise, the rupture cannot reach NPW at $t = t_N$, even if it propagates at V_P after the CCTV site.

We can read $t_N = 48$ from the Fig.4 of Lai et al. (2025), who assumed that the origin time was 2025-03-28 06:20:54 UTC, though a rationale was not provided. This origin time is 2 seconds behind the USGS origin time, suggesting that $t_N = 50$ s may be more appropriate if the USGS time is adopted. If $V_{\rm sup} = V_P = 6$ km/s, the deceleration point and subshear rupture velocity for the earliest ($\tau_P = 3$ s) and latest (the equality in (S.1) holds) cases are $(r_d, V_{\rm sub}) = (98.8, 2.74)$ and $= (65.2, 3.13)$, respectively. Fig.S2b indicates that $V_{\rm sup} \leq 5$ is difficult to achieve, as $V_{\rm sub}$ becomes excessively slow, particularly in the earliest case. Furthermore, $V_{\rm sup} < \sqrt{2}V_S \sim 4.95$ is unstable, as explained in the Discussion section. For numerical simulations, the latest case was employed because $r_d = 65.2$ is more comparable to the local minimum of the surface slip as in Discussion section.

S1.3 2-D kinematic rupture simulation by a boundary element method

We calculated on-fault acceleration during the rupture propagation by 2-D boundary element method. The numerical integration is performed by calculating equation (32) of Tada & Madariaga (2000). In their notation, the flat 2-D crack is along the x_1-axis. We consider strike-slip faulting, where the slip direction and fault-normal direction are along the x_1- and x_2-directions, respectively. Hence, our equation is

$$\dot{u}_2^{i,j,n} = \sum_{k,m} D_1^{k,m} \dot{K}_{1,u2}^{i,j,k,n,m}, . \tag{S.2}$$

Differentiating eq.(S.2) with respect to time yields the acceleration waveform.

The slip-rate function is

$$D_1^{k,m} = \sin^2\left(\frac{\pi}{2}\left(t_m - t_r^k\right)\right) H\left(t_m - t_r^k\right) H\left(t_r^k + 2 - t_m\right), \tag{S.3}$$

where $H(\cdot)$ is the Heaviside function, and t_m is the m-th time collocation point. t_r^k is the rupture arrival time at $x = x_k$, where x_k is the k-th discretized fault segment edge. For Fig.3a and 3b in the main text, we employed the following two scenarios, respectively, with some parameters obtained in S1.2:

- If the rupture velocity is 4.92 km/s (constant) everywhere, then $t_r^k = \dfrac{x_k}{4.92}$.
- If rupture velocity is 3.13 km/s in 65.2 km $< x <$ 124 km and is 6 km/s otherwise, then $t_r^k = \begin{cases} \frac{1}{6}x_k & (0 \leq x_k \leq 65.2) \\ \frac{65.2}{6} + \frac{1}{3}(x_k - 65.2) & (65.2 < x_k < 124) \\ \frac{65.2}{6} + \frac{1}{3}(124 - 65.2) + \frac{1}{6}(x_k - 124) & (124 \leq x_k) \end{cases}.$

S1.4 3-D kinematic rupture simulation by a finite difference method

We numerically solved the equations of motion and constitutive relations for a generalized Zener body using the 3-D parallel finite difference code OpenSWPC (Maeda et al., 2017; Maeda, 2025). A 3-D medium with dimensions of 500 km (north-south) $\times$ 200 km (east-west) $\times$ 100 km (vertical) was discretized using a uniform grid with 100-meter spacing in each direction. The medium was assumed to be a homogeneous, viscoelastic half-space with a mass density of 2.7 g/cm^3, P-wave velocity of 6.0 km/s, S-wave velocity of 3.5 km/s, and intrinsic attenuation factors of Qp = 600 and Qs = 300.

The ground surface was defined at 5 km from the top of the domain, and traction-free boundary conditions (Nakamura et al., 2012) were applied there. The earthquake source was represented as a collection of discrete point sources. A rectangular region in the central part of the model, extending 300 km in the north-south direction and 20 km in depth from the ground surface, was designated as the fault plane. Stress changes associated with fault slip (Coutant et al., 1995; Pitarka, 1999) were applied to the numerical grid points corresponding to the fault for the duration of the rise time starting from the rupture onset time. The rupture onset time at each point was computed according to the setup described in the main text, with rupture initiation assumed at the northern end of the fault. To suppress artificial reflections from the model boundaries, the ADE-CFS perfectly matched layer scheme (Zhang & Shen, 2010) with a thickness of 20 grid points was applied along the outer edges of the computational domain. The model was partitioned into 32×32 segments in the horizontal directions, and the simulation was executed on 256 CPUs. Four MPI processes were launched per CPU, with each process utilizing one-fourth of the CPU's cores via OpenMP threading. The computation of 60,000 time steps with a time increment of 0.005 s took approximately 30 minutes.

S1.5 Estimation of Surface fault slip

We estimated coseismic surface fault slip by pixel-offset (optical correlation) analysis of pre- and post-seismic Sentinel-2 satellite imagery. Here, we used 10 m-resolved Band-3 images of the L2A product, with a central wavelength of 560 nm, obtained on March 20th and 30th, 2025.

For the pixel-offset analysis, we used geoCosiCorr3D (Aati et al., 2022a,b). Here, we employed 32 pixels (320 m) as a window size for correlating the images, and estimated northward and eastward displacement for every eight steps (80 m). Estimated surface displacements were mapped in Fig.S3.

The distribution of surface fault slip (Fig.2b in the main text) was estimated from the discrepancies in northward components between both sides of the surface fault trace, assuming that this component corresponds to the fault displacements, as the fault strike is almost north-south, and the east-west component was negligible. Considering the window size of the pixel-offset analysis, we excluded 1 pixel on the fault trace and 2 pixels (160 m) on each side from the fault in the analysis results. We then calculated the average displacements ranging from 3 to 12 pixels (800 m) on each side of the fault on the east-west cross-sections.

References

Aati, S., Avouac, J.-P., Rupnik, E., & Deseilligny, M.-P. (2022a). Potential and limitation of planetscope images for 2-d and 3-d earth surface monitoring with example of applications to glaciers and earthquakes. *IEEE Transactions on Geoscience and Remote Sensing*, 60, 1–19. https://doi.org/10.1109/tgrs.2022.3215821

Aati, S., Milliner, C., & Avouac, J.-P. (2022b). A new approach for 2-d and 3-d precise measurements of ground deformation from optimized registration and correlation of optical images and ica-based filtering of image geometry artifacts. *Remote Sensing of Environment*, 277, 113038. https://doi.org/10.1016/j.rse.2022.113038

Coutant, O., Virieux, J., & Zollo, A. (1995). Numerical source implementation in a 2d finite difference scheme for wave propagation. *Bulletin of the Seismological Society of America*, 85(5), 1507–1512. https://doi.org/10.1785/BSSA0850051507

Hirano, S. (2025). @Bimaterial. "I analyzed the distance between two edges in the video during surface rupture due to the M7.7 Myanmar earthquake." X. https://x.com/Bimaterial/status/1922157655641952512, posted on May 13, 2025, 5:11 pm, archived at https://archive.md/GJKdo.

Lai, S.-T., Oo, K. M., Htwe, Y. M. M., Yi, T., Than, H. H., Than, O., Min, Z., Oo, T. M., Maung, P. M., Bindi, D., Cotton, F., Evans, P. L., Heinloo, A., Hillmann, L., Saul, J., Sens-Schoenfelder, C., Strollo, A., Tilmann, F., Weatherill, G., Yen, M.-H., Zaccarelli, R., Zieke, T., & Milkereit, C.

(2025). Capacity building enables unique near-fault observations of the destructive 2025 mw 7.7 myanmar earthquake. https://doi.org/10.5194/essd-2025-216

Maeda, T. (2025). *Openswpc/openswpc: Version 25.05.2*. https://doi.org/10.5281/ZENODO.16264099

Maeda, T., Takemura, S., & Furumura, T. (2017). Openswpc: an open-source integrated parallel simulation code for modeling seismic wave propagation in 3d heterogeneous viscoelastic media. *Earth, Planets and Space*, 69(1). https://doi.org/10.1186/s40623-017-0687-2

Nakamura, T., Takenaka, H., Okamoto, T., & Kaneda, Y. (2012). Fdm simulation of seismic-wave propagation for an aftershock of the 2009 suruga bay earthquake: Effects of ocean-bottom topography and seawater layer. *Bulletin of the Seismological Society of America*, 102(6), 2420–2435. https://doi.org/10.1785/0120110356

Pitarka, A. (1999). 3d elastic finite-difference modeling of seismic motion using staggered grids with nonuniform spacing. *Bulletin of the Seismological Society of America*, 89(1), 54–68. https://doi.org/10.1785/bssa0890010054

Styron, R. & Pagani, M. (2020). The gem global active faults database. *Earthquake Spectra*, 36(1_suppl), 160–180. https://doi.org/10.1177/8755293020944182

Tada, T. & Madariaga, R. (2000). Dynamic modelling of the flat 2-d crack by a semi-analytic biem scheme. *International Journal for Numerical Methods in Engineering*, 50(1), 227–251. https://doi.org/10.1002/1097-0207(20010110)50:1<227::aid-nme166>3.0.co;2-5

Zhang, W. & Shen, Y. (2010). Unsplit complex frequency-shifted pml implementation using auxiliary differential equations for seismic wave modeling. *GEOPHYSICS*, 75(4), T141–T154. https://doi.org/10.1190/1.3463431

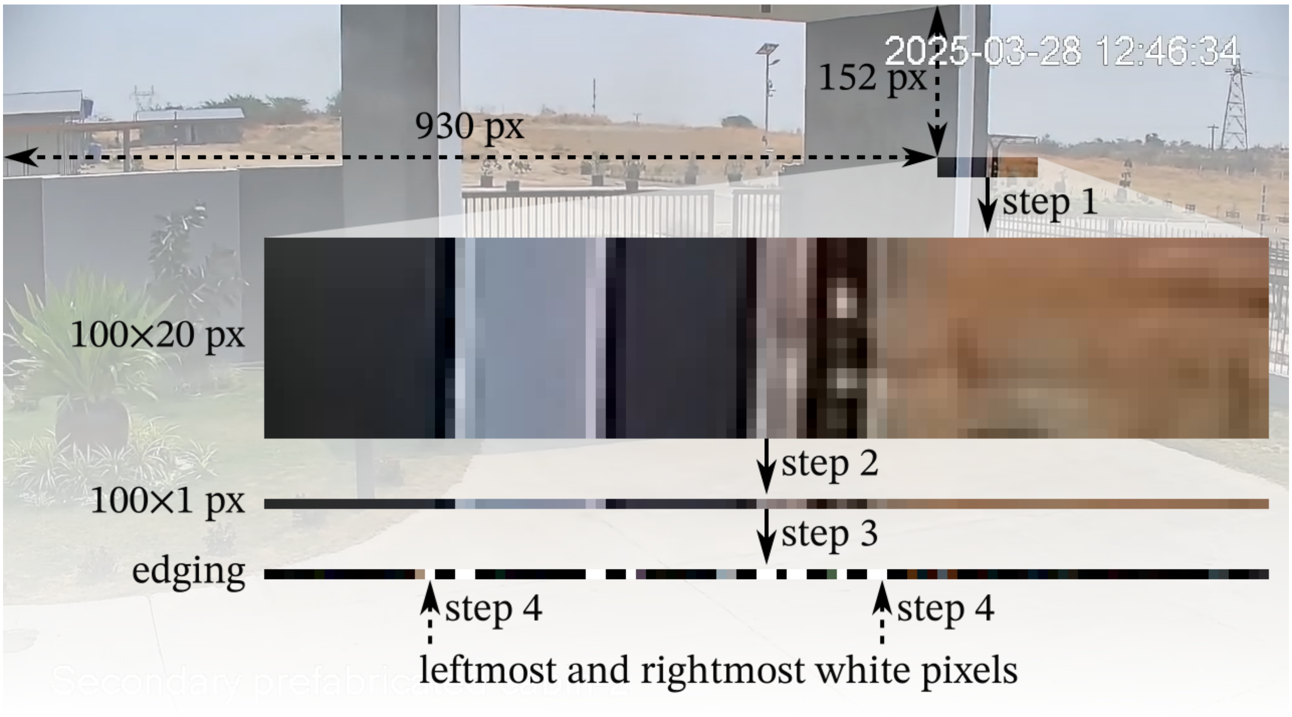

Figure S1: Steps for image analysis to quantify slip history on the surface fault. The leftmost white pixel represents a part of the gate structure in front of the fault, while the rightmost one, a part of a pole on the opposite side.

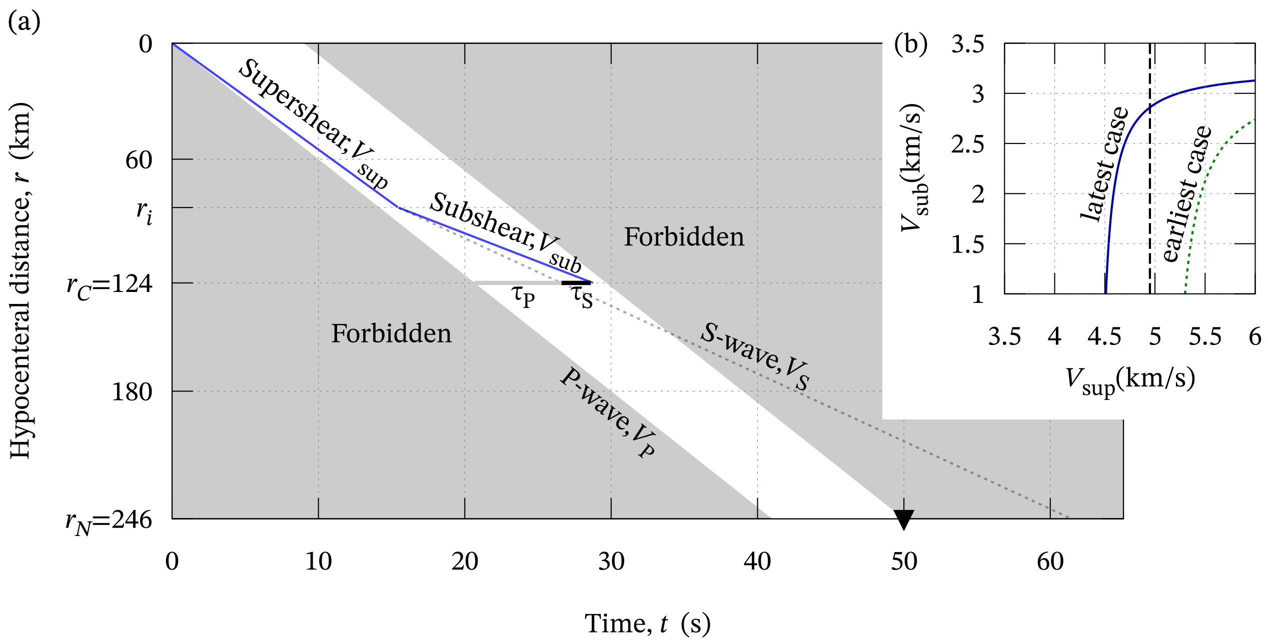

Figure S2: (a) Schematic illustration of possible rupture front to CCTV ($r = r_C$). The rupture front, with a velocity of up to V_P from the origin to the black triangle (NPW), is unable to penetrate the gray-filled regions. At CCTV, the gray (τ_P) and the black (τ_S) horizontal bars correspond to the durations of the P-wave and S-wave, respectively. The deceleration point of the rupture front, r_d, is the intersection of the early supershear rupture front and the S-wave. (b) Subshear rupture velocity as a function of the supershear rupture velocity, V_{sup}. The earliest case corresponds to $\tau_P = 3$ s, while the end of τ_S touches the forbidden region in the latest case. The vertical dashed line in (b) represents $\sqrt{2}V_S$ (see the main text for its meaning).

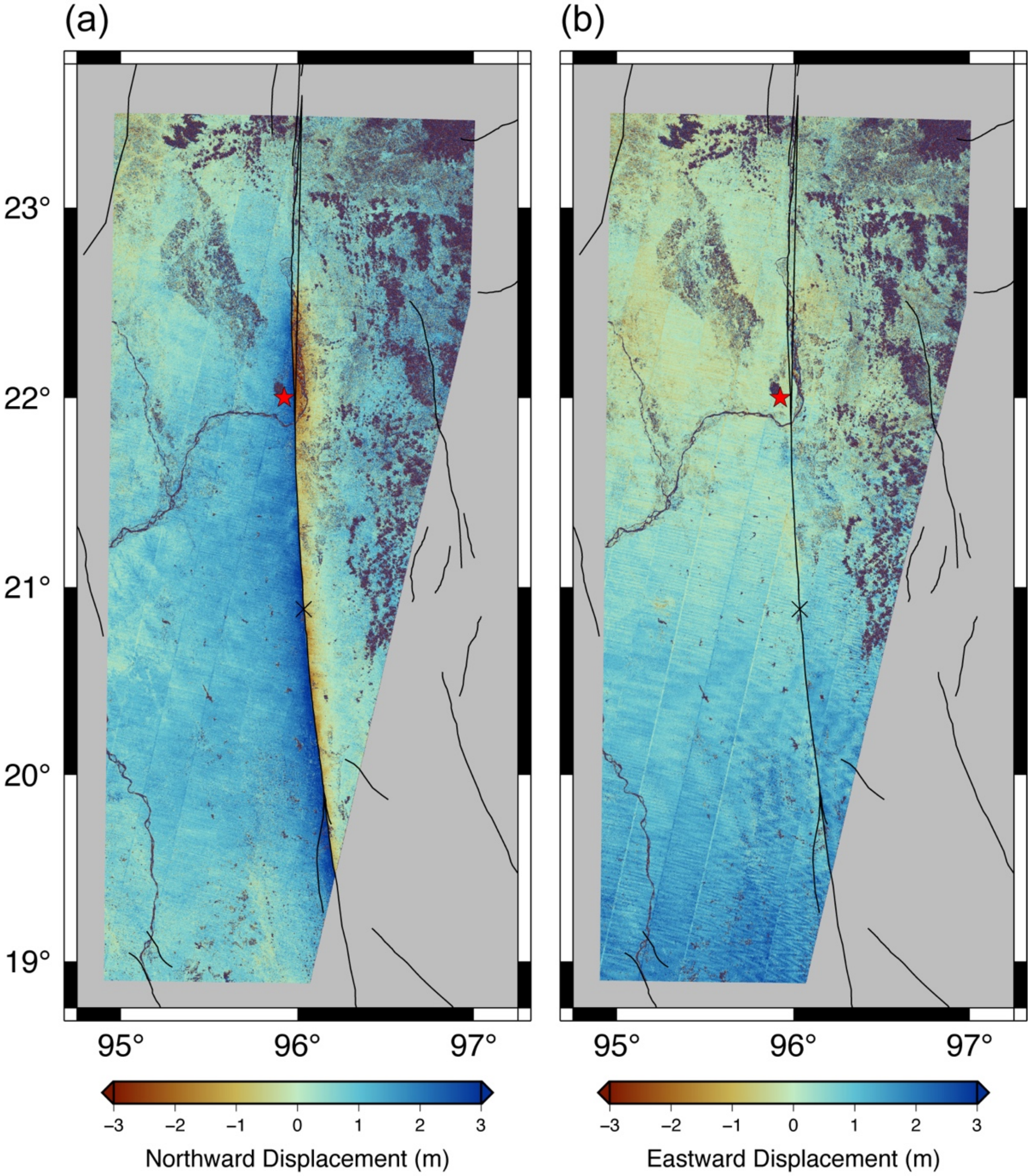

Figure S3: Surface displacement estimated by the pixel-offset (optical correlation) analysis of Sentinel-2 imagery. (a) Northward and (b) Eastward displacements. The red star and the $\times$ mark show the locations of the epicenter and CCTV, respectively. Fault traces are based on Styron & Pagani (2020).